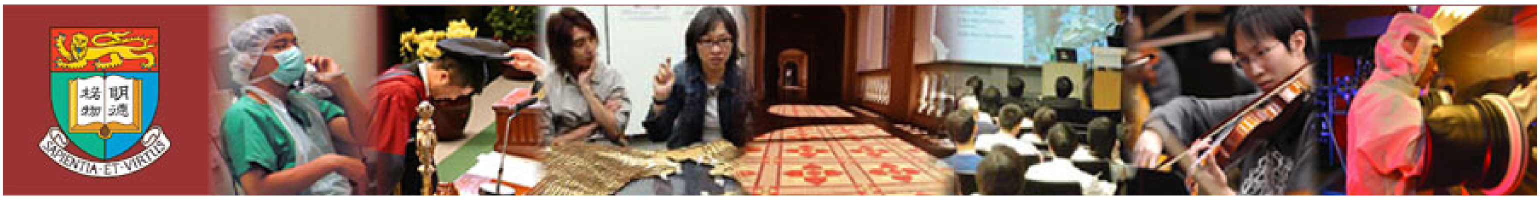

Title	Gate-tunable topological valley transport in bilayer graphene
Author(s)	Sui, M; Chen, G; Ma, L; Shan, WY; Tian, D; Watanabe, K; Taniguchi, T; Jin, X; Yao, W; Xiao, D; Zhang, Y
Citation	Nature Physics, 2015, v. 11 n. 12, p. 1027-1031
Issued Date	2015
URL	http://hdl.handle.net/10722/222006
Rights	This work is licensed under a Creative Commons Attribution-NonCommercial-NoDerivatives 4.0 International License.

Gate-tunable Topological Valley Transport in Bilayer Graphene

Mengqiao Sui[1,2], Guorui Chen[1,2], Liguo Ma[1,2], Wenyu Shan[3], Dai Tian[1,2], Kenji Watanabe[4], Takashi Taniguchi[4], Xiaofeng Jin[1,2], Wang Yao[5], Di Xiao[3] and Yuanbo Zhang[1,2*]

[1]*State Key Laboratory of Surface Physics and Department of Physics, Fudan University, Shanghai 200433, China*

[2]*Collaborative Innovation Center of Advanced Microstructures, Shanghai 200433, China*

[3]*Department of Physics, Carnegie Mellon University, Pittsburgh, Pennsylvania 15213, USA*

[4]*Advanced Materials Laboratory, National Institute for Materials Science, 1-1 Namiki, Tsukuba, 305-0044, Japan.*

[5]*Department of Physics and Center of Theoretical and Computational Physics, University of Hong Kong, Hong Kong, China*

[*]Email: zhyb@fudan.edu.cn

Valley pseudospin, the quantum degree of freedom characterizing the degenerate valleys in energy bands[1], is a distinct feature of two-dimensional Dirac materials[1–5]. Similar to spin, the valley pseudospin is spanned by a time reversal pair of states, though the two valley pseudospin states transform to each other under spatial inversion. The breaking of inversion symmetry induces various valley-contrasted physical properties; for instance, valley-dependent topological transport is of both scientific and technological interests[2–5]. Bilayer graphene (BLG) is a unique system whose intrinsic inversion symmetry can be controllably broken by a perpendicular electric field, offering a rare possibility for continuously tunable valley-topological transport. Here, we used a perpendicular gate electric field to break the inversion symmetry in BLG, and a giant nonlocal response was observed as a result of the topological transport of the valley pseudospin. We further showed that the valley transport is fully tunable by external gates, and that the nonlocal signal persists up to room temperature and over long distances. These observations challenge contemporary understanding of topological transport in a gapped system, and the robust topological transport may lead to future valleytronic applications.

In crystalline solids, a topological current can be induced by the Berry phase of the electronic wave function[6]. Examples include the quantum Hall current in a magnetic field, and the spin Hall current arising from spin-orbit coupling. Such topological transport is robust against impurities and defects in materials – a feature that is much sought after in potential electronic applications. In such applications, the ability to switch and to continuously tune the topological transport is crucial. The topological current is in principle dictated by the crystal symmetry, which is difficult to change in bulk materials. Bilayer graphene, however, offer new opportunities in which inversion symmetry can be controllably broken by an external electric field in the perpendicular direction.

The topological current controlled by the inversion symmetry breaking is associated with carriers' valley pseudospin, which characterises the two-fold degenerate band-edges located at the corners of the hexagonal Brillouin zone. The topological Hall current, odd under time-reversal but even under inversion, is strictly zero in pristine mono- and bi-layer graphene which respect both symmetries. When the inversion symmetry is broken, however, time-reversal symmetry requires the Hall currents to have opposite signs and equal magnitudes in the two valleys (*i.e.*, a valley Hall effect), as recently demonstrated in monolayer graphene in ref 4. Microscopically, inversion symmetry breaking opens a band gap at the charge neutral point (CNP), and produces valley-contrasted Berry curvatures[2]. The Berry curvatures act similarly to a momentum-space magnetic field that causes the Hall effect at finite doping[6]. In BLG, the inversion symmetry (and the Berry curvature) is for the first time controlled by gate electric field. Valley Hall current is therefore expected to be fully tunable by external gates, bringing topological transport in line with modern electronic technology.

In this study, we demonstrated tunable topological valley Hall transport in gate-biased BLG with nonlocal measurement in a Hall bar configuration (Fig. 1a and Fig. 1c inset), which has been used to detect nonlocal transport in other spin/pseudospin systems[4,7–10]. The charge current injected at one end of Hall bar induced a pure valley Hall current in the transverse direction and, because of the inverse valley Hall effect, converted to a charge imbalance at the other end of the sample; we therefore detected a nonlocal response as a voltage drop. We demonstrated that the giant, tunable, nonlocal response can be induced by the perpendicular gate electric field, but is absent in the gapless BLG in which inversion symmetry is present. Such gate tunability indicates the essential role of inversion symmetry breaking in nonlocal transport, and provides unambiguous evidence that our nonlocal signal was a result of the valley Hall effect. The nonlocal transport persists up to room temperature and over long distances (up to 10 μm). Our results represent major progress in the quest for a robust, tunable valley pseudospin system among various alternatives [3–5,11,12], and indicate the possibility of using the nonlocal topological transport in practical applications under ambient conditions.

The structure of our dual-gate graphene field-effect transistors (FETs) is shown in Fig. 1a and 1b. We constructed the device by sequentially transferring BLG and hexagonal boron nitride (hBN) flakes onto an hBN substrate supported on a SiO_2/Si wafer (SiO_2 thickness = 300 nm). Prior to the deposition of the top hBN flake, BLG was etched into a well-defined Hall bar geometry (Fig. 1a, broken line) for easy characterisation in both local and nonlocal configurations. The whole stack was etched again after the deposition of the top hBN to expose the graphene edge for making electrical contacts with metallic leads[13] (Cr/Au, 8 nm and 70 nm, respectively). The final device had BLG sandwiched between the top and bottom gates (Fig. 1b), and the hBN gate dielectric ensured excellent sample quality (see Methods).

Voltages applied on top and bottom gates (V_t and V_b) enabled us to independently control the gap opening and carrier doping in the BLG. The bandgap E_g is determined by the average of top and bottom gate-induced electrical displacement fields, $D = (D_t + D_b)/2$, which breaks the inversion symmetry of the BLG[14]. The carrier doping n can be tuned by the difference of the two displacement fields, $n = \varepsilon_0(D_t - D_b)$, where ε_0 is the vacuum permittivity. In our experiment, the drain electrode was grounded, and the displacement fields were related to top and bottom gate voltages by $D_t = \varepsilon_t(V_t - V_{t0})/d_t$ and $D_b = \varepsilon_b(V_b - V_{b0})/d_b$, where ε and d are the dielectric constant and thickness of the dielectric layers, respectively, and V_{t0} and V_{b0} are effective offset voltages caused by environment-induced carrier doping. The resistance of our sample measured in a standard four-terminal setup (referred to as local resistance R_L) exhibited the typical bebaviour of BLG: the CNP manifested as a peak in R_L as the carrier density is varied in a pristine sample (Fig. 1c, blue), and the peak value increased substantially as a bandgap was opened by a finite field D (Fig. 2a-d, blue). R_L plotted as a function of both V_t and V_b shows the effect of gate bias more clearly in Fig. 2b. Along the line defined by the (V_t, V_b) pairs at the CNP, the bandgap is fully tuned by D, whereas the sample remained charge neutral. The sample exhibited a net charge doping perpendicular to the line in the (V_t, V_b) plane, with the bandgap remaining constant.

A pronounced nonlocal response appeared as the bandgap opens in BLG at low temperatures. We detected the response by sending a current I through the local leads, and sensing the nonlocal voltage V_{NL} at the far end of the sample (see Fig. 1c inset for the measurement setup). The nonlocal resistance R_{NL}, defined as $R_{NL} = V_{NL}/I$, is negligible in a pristine sample with zero gap opening (Fig. 1c, orange). A peak in R_{NL}, however, appeared at a threshold displacement field of $D = 0.28$ V/nm, and increased rapidly to the order of a few hundred Ω at large D (Fig. 2a-d, data obtained at temperature $T = 70$ K). The two-dimensional plot of R_{NL} as a function of V_t and V_b shows the general behavior of the nonlocal response at $T = 70$ K. R_{NL} generally peaks at the CNP, but two features distinguish the behavior of R_{NL} from that of the local resistance R_L: the R_{NL} peak is generally sharper than the R_L peak, and R_{NL} drops to zero outside of the peak whereas R_L maintains an order of approximately 100 kΩ at finite doping. Both features indicate the distinct origins of R_{NL} and R_L, and are general behavior of nonlocal transport observed in other graphene pseudospin and spin systems[4,7,9]. In the present study, we noted that the peak positions of R_{NL} and R_L were not always aligned with each other; we attribute the misalignment to inhomogeneities that were present in our samples (Supplementary Section IV). We emphasise that the observed R_{NL} was not from the stray charge current that contributes an ohmic nonlocal resistance[7]. Such ohmic contribution decreases exponentially with the sample length-to-width ratio L/w, and is up to two orders of magnitude lower than the observed R_{NL} in the device shown in Fig. 2a-d ($L = 5$ μm and $w = 1.5$ μm; the ohmic contribution to R_{NL} is represented by the broken line). A pronounced nonlocal signal was observed in devices with an even higher L/w ratio of up to 6.7 (Fig. 3e).

The temperature dependence of R_{NL} and R_L revealed crucial information on the microscopic mechanism of both the local and nonlocal transport. Three distinct transport regimes were observed at large fields (Fig. 3a): thermal activation at high temperature; nearest-neighbor hopping at intermediate temperature; and variable-range hopping at low temperature. These transport regimes were consistent with previous studies[15,16] (Supplementary Section V). In particular, the high-temperature activation behaviour enabled us to extract the BLG bandgap E_g as a function of D, which agreed well with theoretical calculations and previous measurements[14,17] (Fig. 3a inset and Supplementary Section V).

Pronounced nonlocal signal is observed in both thermal activation and hopping regimes (Fig. 3b). We found that R_{NL} also followed an exponential activated behavior in the thermal activation regime at high temperatures (Fig. 3b inset), although with an exponent higher than E_g/k_BT (Supplementary Fig. 5d). The connection between R_{NL} and R_L became obvious when $\ln R_{NL}$ was plotted against $\ln R_L$ (Fig. 3c). Data sets for different D were all in straight lines with the same slope $\alpha = 2.77 \pm 0.02$ in the thermal activation regime; hence, a simple relation $R_{NL}{\sim}R_L^{\alpha}$ can be established. We noted that a diffusive nonlocal topological transport model indeed predicted a power law relation $R_{NL}{\sim}R_L^3\sigma_{xy}^2e^{-L/\lambda_v}/\lambda_v$ (ref. 18), where σ_{xy} is the valley Hall conductivity, and λ_v is the valley diffusion length. Our observation agreed reasonably well with this predicted scaling between R_{NL} and R_L, and the deviation of α from 3 may indicate the complicated role of σ_{xy} and/or λ_v in R_{NL}. α varied among samples, probably as a result of differences in sample disorder (Supplementary Fig. 6). Intriguingly, our data show that the simple relation $R_{NL}{\sim}R_L^{\alpha}$ persists beyond the thermal activation regime and into the hopping regime until the curves eventually level off (Fig. 3c).

The widely tunable bandgap in BLG provides another crucial benefit, which is the room-temperature operation of our BLG nonlocal FET. Fig. 3d displays the R_{NL} observed up to room temperature in a BLG biased at $D = -1.23$ V/nm (corresponding to $E_g = 135$ meV). A wide bandgap alone does not guarantee high-temperature nonlocal transport because the nonlocal signal, along with R_L, decreases exponentially with temperature in the thermal activation regime. However, R_{NL} does not decrease as rapidly with increasing temperature in the hopping regime. When the onset of the hopping regime occurs at high temperatures, room-temperature operation consequently remains possible. The key, therefore, is to find samples in which the onset of the hopping regime occurs at near room temperatures, as we have demonstrated in the samples shown in Fig. 3d and Supplementary Fig. 7.

We now turn to the length dependence of the nonlocal valley transport. Here we note the analog between the valley transport in biased BLG and the spin transport in which spin-flip scattering causes the spin diffusion current to decay exponentially. The valley current in BLG decreases through intervalley scattering, which requires a large momentum transfer (*e.g.*, by atomic scale disorders). Such disorders are found to be extremely rare in cleaved BLG crystals[19,20], implying a large valley diffusion length λ_v[21,22]. In the present study, an appreciable nonlocal signal was observed in samples up to 10 μm long. Fig. 3e shows the length-dependent R_{NL}, measured on a single device under a field of $D = -0.47$ V/nm. From a line fit to the semilog plot of the R_{NL} peak value as a function of sample length (Fig. 3e inset), we obtained an order of magnitude estimation $\lambda_v \sim 1$ μm, because sample inhomogeneity (manifested as shift of R_{NL} peaks in Fig. 3e) preventing a more precise estimation. Such a large length scale agrees reasonably well with recent study on inter-valley scattering[21,22], and is also consistent with the areal density of atomic defects (12.05 μm^{-2}) found in Kish graphite[23], which is the same type of specimen used in this study.

The observation of a giant nonlocal response in the middle of the energy gap in insulating BLG was unexpected. Although midgap helical edge sates in 2D quantum spin Hall systems can support long-range nonlocal conduction[24–26], such spin helical edge states did not exist in our study because BLG is topologically trivial. Midgap valley helical modes may still exist at topological domain walls or edges of BLG in certain circumstances[27–29], and may potentially lead to nonlocal conduction. The nonlocal transport through edge states and bulk states, however, exhibit drastically different length dependence; for a given sample width, bulk conduction depends on the active length of the sample, whereas the edge state conduction depends only on the length of the edge[7]. We took advantage of this difference to fabricate the device shown in Fig. 4 inset: two Hall bars (left and right with shared current injection leads 2 and 5) have the same active sample length but substantially different edge lengths. The fact that a comparable nonlocal response was observed on both Hall bars unambiguously demonstrates the bulk origin of our valley transport. A robust nonlocal response with the same sign and order of magnitude was observed in all the samples we fabricated on hBN (6 in total). Helical modes at the domain walls, which differ according to sample if they exist at all, is unlikely to be the origin of the observed nonlocal transport.

The question then arises as to what physical mechanism leads to the nonlocal valley transport that we observed. The valley Hall effect originally proposed in graphene requires finite doping[2], and is therefore not applicable in our insulating BLG. To this end, we note that nonlocal transport in an insulator without helical edge states is an area still open to theoretical investigation[30], and our results call for continued effort, both experimental and theoretical, to address this outstanding problem.

In conclusion, we observed a giant nonlocal valley Hall effect in BLG subjected to a symmetry-breaking gate electric field. The long-distance valley transport is fully tuned by the gate, and persists up to room temperature at large gate biases. Our observation of bulk valley current in biased BLG opens up new avenues for future experimental and theoretical investigation of the valley/spin Hall effect in the insulating regime. In addition, the demonstration of a gate-tunable valley degree of freedom and nonlocal topological transport is major progress towards the development of valleytronic applications.

Methods

Device fabrication. We fabricated BLG devices by following procedures similar to those described in ref 13 and [31]. BLG flakes transferred onto hBN substrate were etched into Hall bar geometry by using standard electron beam (ebeam) lithography followed by reactive ion etch. The etched BLG Hall bar was then annealed at 370 ℃ in an Ar/H_2 atmosphere overnight to remove ebeam resist residue. We further cleaned the sample surface by using atomic force microscope (Park Systems) operating in contact mode. The BLG Hall bar on the hBN substrate was then covered by another layer of hBN as a top-gate dielectric. The hBN/BLG/hBN stack was then etched using inductively coupled plasma (ICP) to expose graphene leads at the edge. Finally, metal electrodes (Cr/Au, 8 nm and 70 nm) were deposited for electrical contact with graphene leads. The devices exhibited mobility ranging from 1,500 cm^2/Vs to 50,000 cm^2/Vs at 10 K, and nonlocal signal was observed in all of them.

Nonlocal resistance measurement. The high common-mode voltage present in the measurement circuit and the high output impedance of the nonlocal voltage signal cause the typical lock-in measurement to fail at large gate biases when BLG becomes excessively resistive. We found that the problem can be mitigated by increasing the input impedance of the preamplifier of the measurement circuit. Reliable measurement of the nonlocal signal can also be obtained by detecting the current instead of voltage in the nonlocal leads; however, precautions must be taken to float the current preamplifier. A detailed discussion of our nonlocal measurement is presented in Supplementary Section I.

References

1. Xu, X., Yao, W., Xiao, D. & Heinz, T. F. Spin and pseudospins in layered transition metal dichalcogenides. *Nat. Phys.* **10,** 343–350 (2014).
2. Xiao, D., Yao, W. & Niu, Q. Valley-Contrasting Physics in Graphene: Magnetic Moment and Topological Transport. *Phys. Rev. Lett.* **99,** 236809 (2007).
3. Mak, K. F., McGill, K. L., Park, J. & McEuen, P. L. The valley Hall effect in MoS2 transistors. *Science* **344,** 1489–1492 (2014).
4. Gorbachev, R. V. *et al.* Detecting topological currents in graphene superlattices. *Science* **346,** 448–451 (2014).
5. Xiao, D., Liu, G.-B., Feng, W., Xu, X. & Yao, W. Coupled Spin and Valley Physics in Monolayers of MoS2 and Other Group-VI Dichalcogenides. *Phys. Rev. Lett.* **108,** 196802 (2012).
6. Xiao, D., Chang, M.-C. & Niu, Q. Berry phase effects on electronic properties. *Rev. Mod. Phys.* **82,** 1959–2007 (2010).
7. Abanin, D. A. *et al.* Giant Nonlocality Near the Dirac Point in Graphene. *Science* **332,** 328–330 (2011).
8. Hoffmann, A. Spin Hall Effects in Metals. *IEEE Trans. Magn.* **49,** 5172–5193 (2013).
9. Balakrishnan, J., Kok Wai Koon, G., Jaiswal, M., Castro Neto, A. H. & Özyilmaz, B. Colossal enhancement of spin-orbit coupling in weakly hydrogenated graphene. *Nat. Phys.* **9,** 284–287 (2013).
10. Wang, Z., Tang, C., Sachs, R., Barlas, Y. & Shi, J. Proximity-Induced Ferromagnetism in Graphene Revealed by the Anomalous Hall Effect. *Phys. Rev. Lett.* **114,** 016603 (2015).

11. Yao, W., Xiao, D. & Niu, Q. Valley-dependent optoelectronics from inversion symmetry breaking. *Phys. Rev. B* **77,** 235406 (2008).

12. Wu, S. *et al.* Electrical tuning of valley magnetic moment through symmetry control in bilayer MoS2. *Nat. Phys.* **9,** 149–153 (2013).

13. Wang, L. *et al.* One-Dimensional Electrical Contact to a Two-Dimensional Material. *Science* **342,** 614–617 (2013).

14. Zhang, Y. *et al.* Direct observation of a widely tunable bandgap in bilayer graphene. *Nature* **459,** 820–823 (2009).

15. Zou, K. & Zhu, J. Transport in gapped bilayer graphene: The role of potential fluctuations. *Phys. Rev. B* **82,** 081407 (2010).

16. Taychatanapat, T. & Jarillo-Herrero, P. Electronic Transport in Dual-Gated Bilayer Graphene at Large Displacement Fields. *Phys. Rev. Lett.* **105,** 166601 (2010).

17. Zhu, J. Transport in bilayer and trilayer graphene: band gap engineering and band structure tuning. in *http://meetings.aps.org/link/BAPS.2014.MAR.B30.1*

18. Abanin, D. A., Shytov, A. V., Levitov, L. S. & Halperin, B. I. Nonlocal charge transport mediated by spin diffusion in the spin Hall effect regime. *Phys. Rev. B* **79,** 035304 (2009).

19. Decker, R. *et al.* Local Electronic Properties of Graphene on a BN Substrate via Scanning Tunneling Microscopy. *Nano Lett.* **11,** 2291–2295 (2011).

20. Xue, J. *et al.* Scanning tunnelling microscopy and spectroscopy of ultra-flat graphene on hexagonal boron nitride. *Nat. Mater.* **10,** 282–285 (2011).

21. Engels, S. *et al.* Limitations to Carrier Mobility and Phase-Coherent Transport in Bilayer Graphene. *Phys. Rev. Lett.* **113,** 126801 (2014).

22. Couto, N. J. G. *et al.* Random Strain Fluctuations as Dominant Disorder Source for High-Quality On-Substrate Graphene Devices. *Phys. Rev. X* **4,** 041019 (2014).

23. Wu, S., Yang, R., Shi, D. & Zhang, G. Identification of structural defects in graphitic materials by gas-phase anisotropic etching. *Nanoscale* **4,** 2005–2009 (2012).

24. König, M. *et al.* Quantum Spin Hall Insulator State in HgTe Quantum Wells. *Science* **318,** 766–770 (2007).

25. Roth, A. *et al.* Nonlocal Transport in the Quantum Spin Hall State. *Science* **325,** 294–297 (2009).

26. Bernevig, B. A., Hughes, T. L. & Zhang, S.-C. Quantum Spin Hall Effect and Topological Phase Transition in HgTe Quantum Wells. *Science* **314,** 1757–1761 (2006).

27. Yao, W., Yang, S. A. & Niu, Q. Edge States in Graphene: From Gapped Flat-Band to Gapless Chiral Modes. *Phys. Rev. Lett.* **102,** 096801 (2009).

28. Li, J., Martin, I., Büttiker, M. & Morpurgo, A. F. Topological origin of subgap conductance in insulating bilayer graphene. *Nat. Phys.* **7,** 38–42 (2011).

29. Alden, J. S. *et al.* Strain solitons and topological defects in bilayer graphene. *Proc. Natl. Acad. Sci.* **110,** 11256–11260 (2013).

30. Lensky, Y. D., Song, J. C. W., Samutpraphoot, P. & Levitov, L. S. Topological Valley Currents in Gapped Dirac Materials. *ArXiv14121808 Cond-Mat* (2014). at <http://arxiv.org/abs/1412.1808>

31. Taychatanapat, T., Watanabe, K., Taniguchi, T. & Jarillo-Herrero, P. Quantum Hall effect and Landau-level crossing of Dirac fermions in trilayer graphene. *Nat. Phys.* **7,** 621–625 (2011).

Acknowledgements

We thank Q. Niu, D.-H. Lee, F. Wang, J. Shi, J. Xiao, J. Zhu for the discussions. Part of the sample fabrication was performed at the Fudan Nano-fabrication Lab. M.S., G.C., L.M. and Y.Z. acknowledge the financial support of the National Basic Research Program of China (973 Program) under the grant nos. 2013CB921902 and 2011CB921802, and NSF of China under the grant nos. 11034001 and 11425415. W.Y. acknowledges the support from the University of Hong Kong (OYRA), and the RGC of Hong Kong SAR (HKU706412P). W.S. and D.X. acknowledge the support from the U.S. Department of Energy, Office of Science, Office of Basic Energy Science, under award no. DE-SC0012509.

Figure captions

Figure 1 | Dual-gated BLG FET and its local and nonlocal characterisation. a, Optical image of a typical BLG FET viewed from the top. A BLG Hall bar (outlined by a broken line) is sandwiched between the top and bottom hBN flakes. The hBN/BLG/hBN stack (blue) was etched to expose the BLG leads at the edge which are subsequently contacted by Au electrodes (orange). **b**, Schematic cross-sectional view of the device shown in **a**. An Au pad and degenerately doped silicon served as top and bottom gate, respectively. **c**, Local and nonlocal resistance measured as a function of top-gate voltage V_t while the bottom-gate voltage V_b was fixed at zero. BLG should have a zero bandgap at the CNP, and nonlocal signal was not detected under this condition. Inset: Illustration of the local and nonlocal measurement setup.

Figure 2 | Local and nonlocal response of biased BLG. a-d, Local and nonlocal resistance as a function of V_t with V_b fixed at varying voltages. The length and width of the sample were 5 μm and 1.5 μm, respectively. The broken lines show the expected ohmic nonlocal contribution (see text), which is substantially smaller than the actual measured R_{NL} (orange curves). **e** and **f**, local and nonlocal resistance measured as a function of both V_t and V_b. Data were obtained from the same device measured in **a-d**. The crosses mark the point $(V_{t0}, V_{b0}) = (1.3V, -7.5V)$ where no bandgap opened in BLG. All data were recorded at $T = 70$ K.

Figure 3 | Temperature and length dependence of the local and nonlocal responses of biased BLG a, Peak resistance in R_L measured as a function of temperature under varying electric displacement fields. Three transport regimes are clearly visible for displacement field $D > 0.5$V/nm (see text). Inset: The Arrhenius plot of R_L showing thermal activation behavior at high temperatures. Broken lines are the line fit to the linear part of the Arrhenius plot, and thermal activation energy could be obtained from the slope of the line fit (Supplementary Section V). The triangles mark the onset of hoping regime. **b**, Peak nonlocal resistance in R_{NL} measured as a function of temperature under varying electric displacement fields. Data were obtained from the same device measured in **a**. Inset: The Arrhenius plot of R_{NL}. R_{NL} also shows thermal activation behavior at high temperatures, and broken lines are the line fit. **c**, $\ln R_L$ plotted against $\ln R_{NL}$ for varying displacement field D. R_{NL} and R_L are from the data sets in **a** and **b**. Triangles mark the onset of hoping regime shown in **a**. $\ln R_L$ scales linearly with $\ln R_{NL}$ with a single slope $\alpha = 2.77 \pm 0.02$ for different D in both thermal activation and hopping regimes, before leveling off deep in the hopping regime. The broken lines are the line fit to the linear part of the data sets. **d**, High-temperature

R_{NL} obtained in a sample in which the onset of hopping regime occurred at near room-temperature (see text). The curves are shifted for clarity. The broken lines are a visual guide. The back gate was fixed at $V_b = -100$ V. **e**, Length dependence of nonlocal response. Hall bars with different length L were fabricated on a single a device. R_{NL} was measured at different L with $\mathrm{V}_b = 30$ V and $\mathrm{T} = 20$ K. Sample width: 1.5 μm. Inset: Semilog plot of peak values of R_{NL} as a function of L. The broken line is a visual guide that corresponds to a valley diffusion length of approximately 1 μm.

Figure 4 | Bulk v.s. edge nonlocal transport. Nonlocal resistance as a function of V_t (V_b fixed at 50 V) obtained on two Hall bars (left and right) shown in the inset. Data were obtained at $\mathrm{T} = 30$ K. The two Hall bars share two local leads (2 and 5) in the middle, and the left and right Hall bar have the same active sample length but substantially different edge lengths. We passed current through the two local leads and measure R_{NL} at the far end of the left Hall bar (contact 1 and 4) and right Hall bar (contact 3 and 6). Nonlocal signal was detected with similar amplitude on both the left and right Hall bars, indicating the bulk origin of the nonlocal transport. Inset: BLG sample on an hBN substrate before deposition of the top hBN flake. The purple dashed line outlines the geometry of etched BLG, and the yellow dashed lines indicate the position of the electrodes to be deposited.

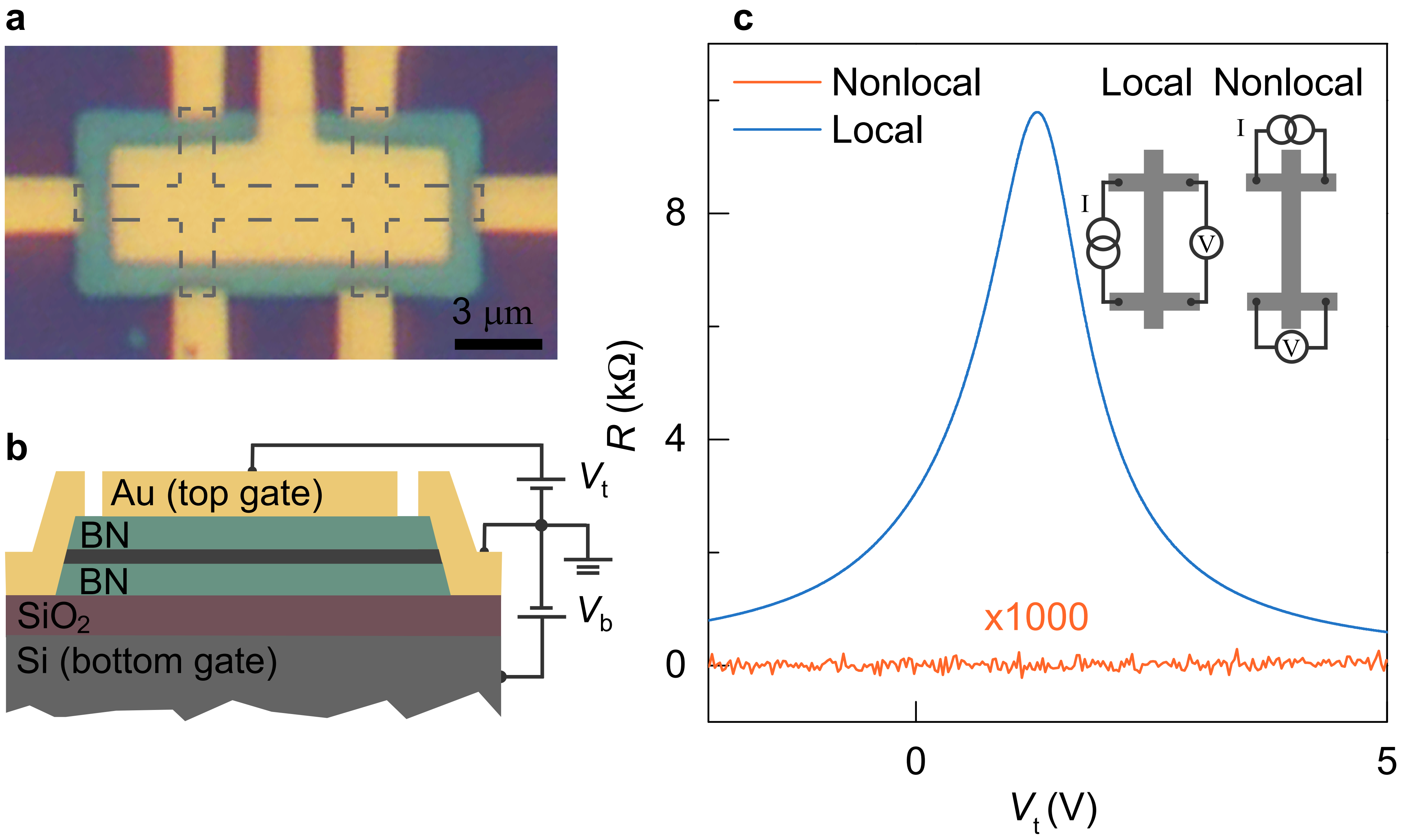

Fig. 1, M. Sui *et al*

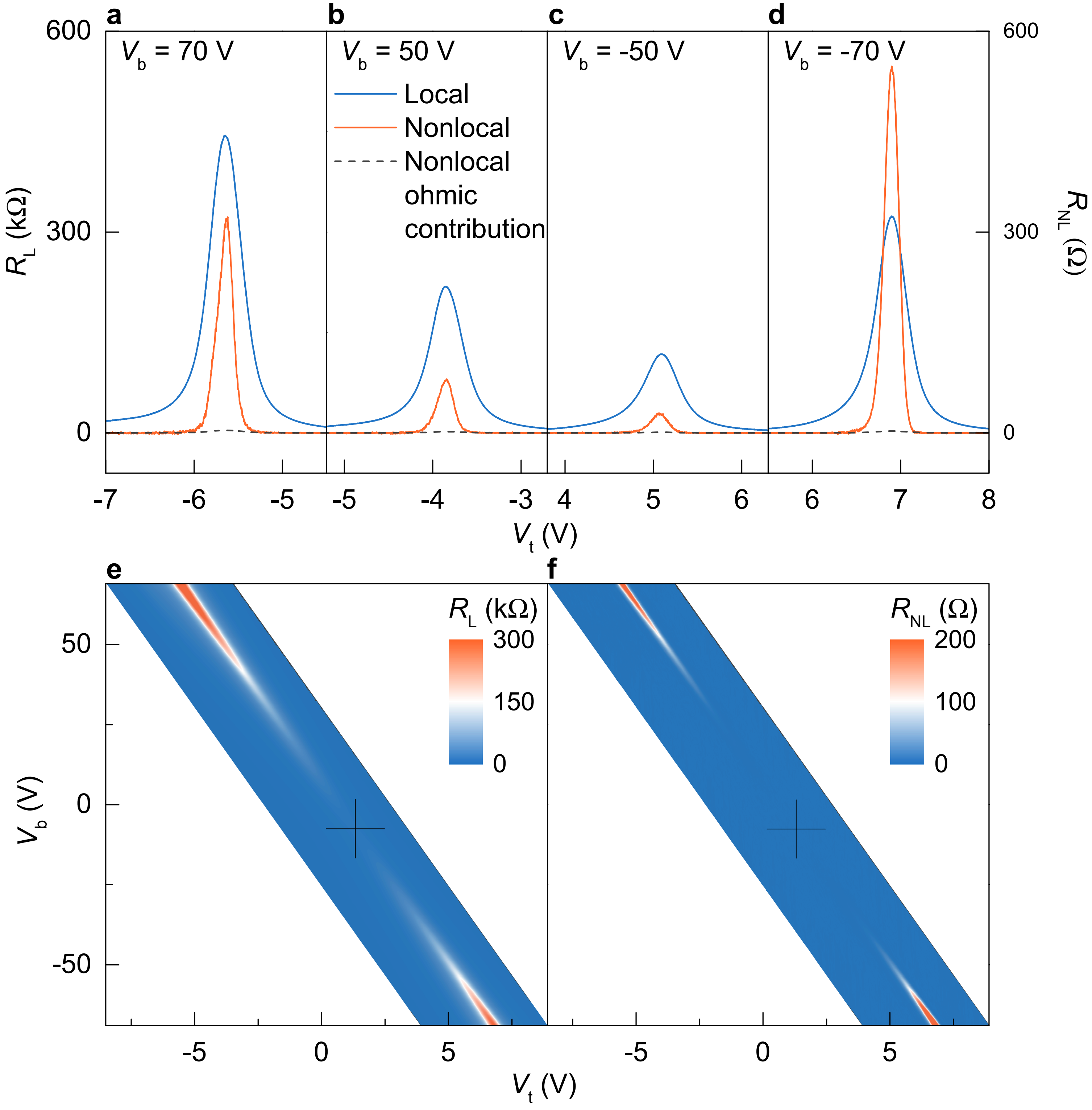

Fig. 2, M. Sui *et al*

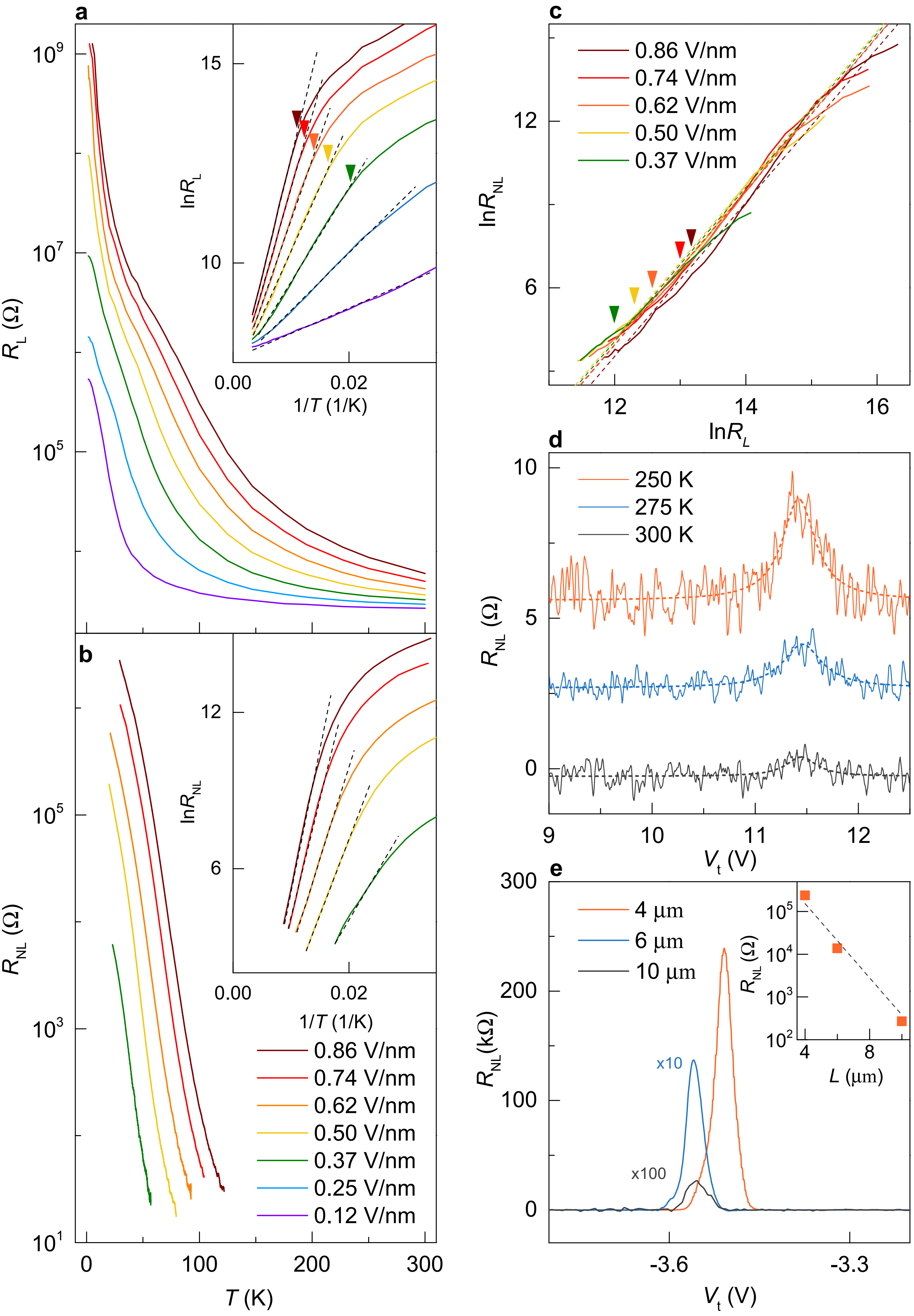

Fig. 3, M. Sui *et al*

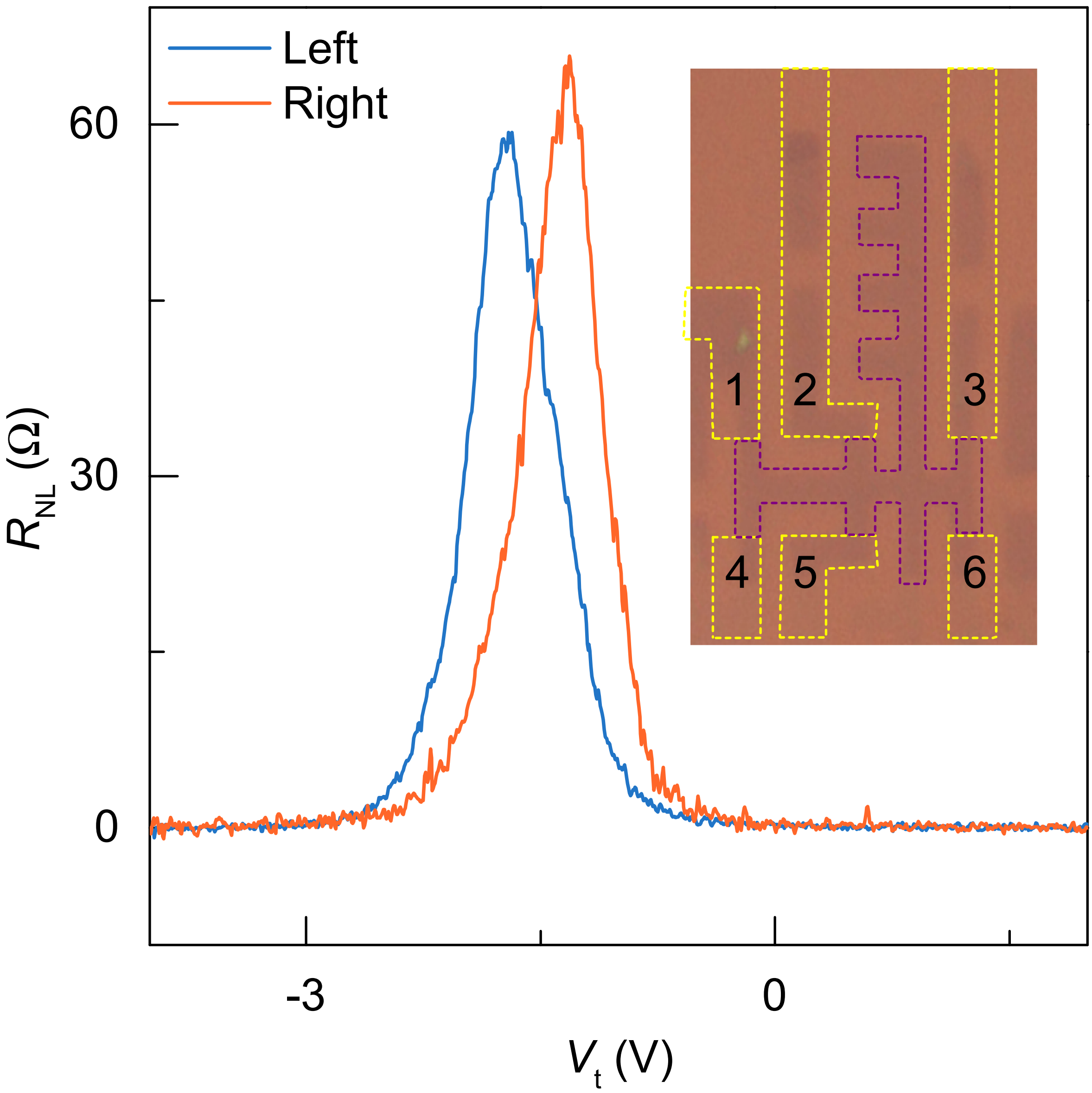

Fig. 4, M. Sui *et al*

Supplementary Information for

Gate-tunable Topological Valley Transport in Bilayer Graphene

Mengqiao Sui, Guorui Chen, Liguo Ma, Wenyu Shan, Dai Tian, Kenji Watanabe,

Takashi Taniguchi, Xiaofeng Jin, Wang Yao, Di Xiao and Yuanbo Zhang*

*Email: zhyb@fudan.edu.cn

Content

I. Measurement schemes to eliminate artifacts in nonlocal detection

Measurement artifacts may appear when typical lock-in measurement setup (shown in Fig. S2b) is used for detection. An example of the artifact is shown in Fig. S1a, where the peak in R_{NL} are distorted and negative R_{NL} appears. We found that the spurious signal was from the measurement setup, as we shall discuss below.

The spurious signal came from the common mode voltage V_{CM} at the current injection side of the Hall bar (marked by the red dot in Fig. S1b). Since lock-in amplifier input typically has a single-ended input resistance of $R_{input}\sim 10\ \text{M}\Omega$ to the ground (we use Stanford Research Systems SR830), V_{CM} induces current through the two nonlocal leads (3 and 4 in Fig. S1b). Resistance imbalance between the two nonlocal leads could therefore induce a spurious voltage difference at the input of the lock-in amplifier:

$$V_{NL}^{s} = \frac{V_{CM}R_A}{R_{input}+R_A} - \frac{V_{CM}R_B}{R_{input}+R_B} \approx (R_A - R_B)\frac{V_{CM}}{R_{input}} \qquad (1)$$

where R_A and R_B are the total resistance from cross at the local side of the Hall bar (red dot in Fig. S1b) to the input of the lock-in amplifier. R_A and R_B include BG resistance, contact resistance at the nonlocal electrodes (3 and 4 in Fig. S1b), and resistance of the voltage leads, and are typically on the order of 1 MΩ. In a typical measurement, $\mathrm{V_{CM}} \approx 10\ \text{mV}$ assuming a sample resistance on order of $1\ \text{M}\Omega$ and current excitation of $10\ \text{nA}$. A difference of $\sim 10\ \text{k}\Omega$ in R_A and R_B, which is also typical, would introduce a V_{NL}^{s} on the order of $\sim 1\ \mu\text{V}$. Such a spurious voltage is on the same order of magnitude as the real valley Hall nonlocal signal, and is indeed what we have measured in Fig. S1a. We note that incomplete rejection of V_{CM} at the lock-in pre-amplifier, as well as the capacitive coupling between the voltage probe leads, could also induce spurious effects in principle. Those effects, however, can be suppressed 1) by the high common mode rejection ratio $\sim 10^5$ found in typical lock-ins, and 2) by operating the lock-in at low frequencies (~ 3 Hz in our case).

The spurious voltage V_{NL}^{s} can be eliminated by careful design of the measurement setup. Here we describe three measurement schemes that are able to detect true nonlocal valley Hall signal without distortion.

First, V_{NL}^{s} can be reduced by increasing the input impedance of the voltage meter, as is apparent in Eq. (1). This can be achieved by replacing lock-in amplifier with high input impedance voltage meters such as Keithley 2182A nanovoltmeter ($R_{input} > 10\ \text{G}\Omega$) as shown in Fig. S1c. We found that the nanovoltmeter, used in combination with Keithley 6221 precision current source operating in delta mode, yielded satisfactory measurement results as shown in Fig. S1f (Method A).

Second, V_{NL}^{s} can also be reduced by suppressing V_{CM}. To this end, we took advantage of a feedback circuit consisting of an operational amplifier (OPA), and devised a measurement setup schematically shown in Fig. S1d. The OPA kept the voltage level at the cross center (marked by blue dot in Fig. S1d) at zero while maintaining the same current flow, so the measurement circuit was not disturbed. We confirmed that this method suppresses V_{CM} down to $< 1\ \mu\text{V}$, and gave a good measurement of R_{NL} as shown in Fig. S1f (Method B).

Third, the effect of V_{CM} can be eliminated altogether by floating the nonlocal signal detection setup, and measuring the nonlocal current instead of voltage as illustrated in (Fig. S1e). To float the current amplifier (DL Instruments Ithaco Model 1211), we powered it with battery, and used an optical isolator to retrieve the output signal without bridging the ground. The nonlocal voltage (Fig. S1f, Method C) was then obtained by multiplying the measured nonlocal current with the internal impedance of the nonlocal signal.

The three independent measurement gave consistent nonlocal measurement results (Fig. S1f). The excellent agreement among them indicated that the spurious voltage V_{NL}^{s} can be effectively suppressed.

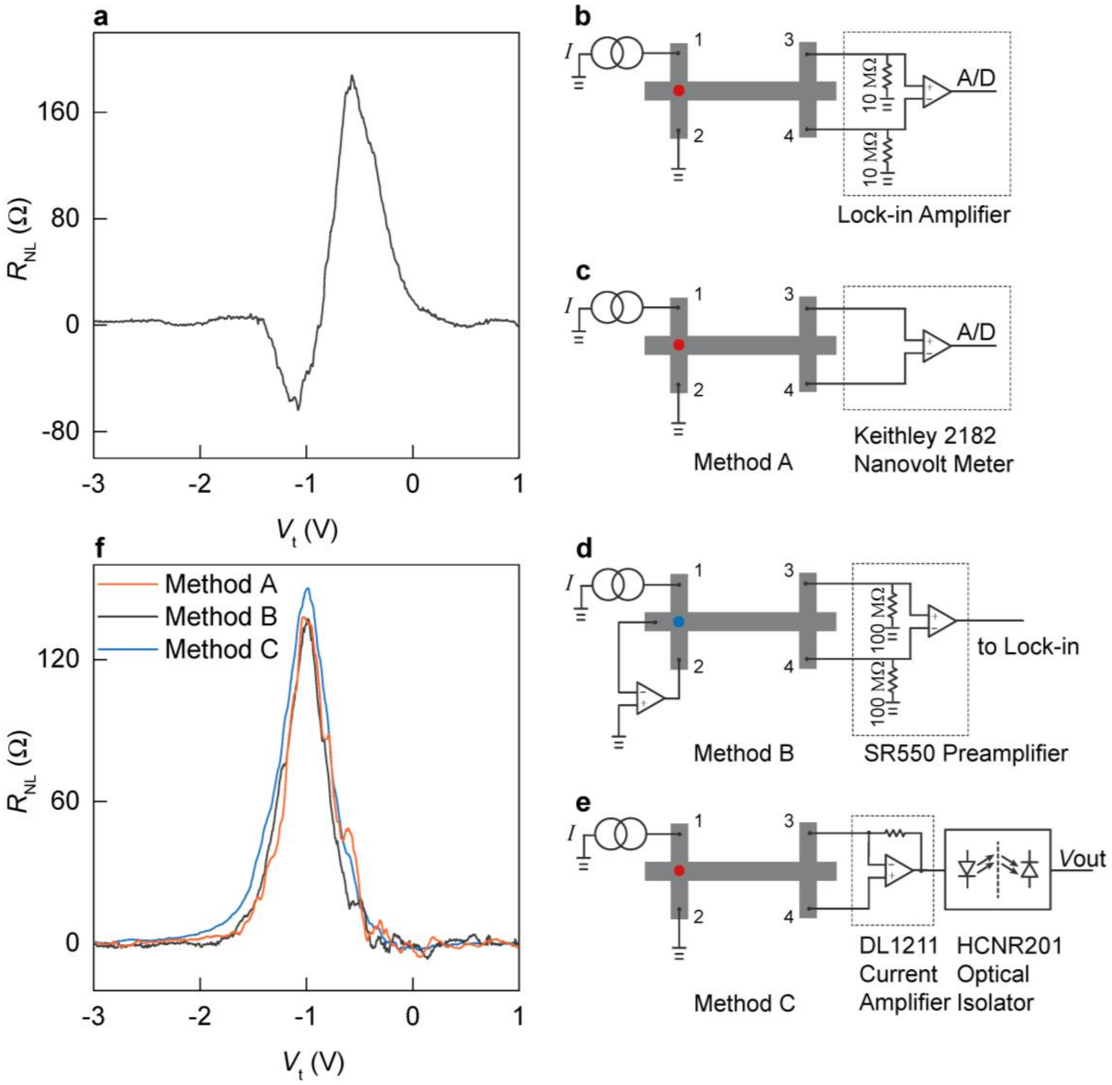

Supplementary Figure 1 | Nonlocal measurement schemes to eliminate spurious signal. **a**, Nonlocal resistance R_{NL} as a function of top gate voltage V_t obtained from typical lock-in measurement. The valley Hall signal mixed with spurious signal to produce the curve shown here. **b**, Nonlocal voltage measurement with typical lock-in amplifier (typical input impedance of $R_{input} \sim 10\ \mathrm{M\Omega}$). **c**, Nonlocal voltage measurement with Keithley 2182A nanovoltmeter ($R_{input} > 10\ \mathrm{G\Omega}$). **d**, Nonlocal voltage measurement with voltage preamplifier (Stanford Research Systems, Model SR550), while the common mode voltage V_{NL}^{s} is suppressed by a voltage-balancing OPA. **e**, Nonlocal current measurement with a floated current amplifier. The output of the amplifier is transmitted through an optical isolator to keep the amplifier floated. **f**, R_{NL} as a function of V_t obtained using the methods described in **c**, **d** and **e**. The sample is the same as in **a**, but the spurious signal is now eliminated from the measurements. The results from three independent measurements agree with each other well.

II. Characterizing nonlocal voltage signal

We provide basic characterization of the nonlocal voltage signal in this section. To ensure reliable nonlocal voltage measurement, we made sure that the electrical contacts to BG was ohmic. This is shown in Fig. S2a, where the linear I-V characteristics at the CNP of biased BG indicate that the contacts remain ohmic even when BG is gapped. The measurement was done at $T = 70$ K, the same temperature where our nonlocal measurements in Fig. 2 were performed.

We then performed a set of basic checks on the nonlocal voltage measurements to rule out artifacts potentially from other sources such as heating effect[1]. The nonlocal voltage changed its sign when the local current injection was reversed (Fig. S2b), indicating that heating effect was negligible in our setup. We also checked the 2f output in our lock-in measurement, did not observe discernable signal from heating effect. In addition, our nonlocal measurement satisfied the universal reciprocal relation, i.e. we observed the same signal if the current and voltage probes were switched (Fig. S2b).

Finally, we characterized the output impedance of the nonlocal voltage. In the measurement setup shown in Fig. S2c, nonlocal current is a function of a known external resistance R_0 we add in the circuit:

$$I_{NL} = \frac{IR_{NL}}{R_0 + R_s} \tag{2}$$

where R_s represents the output impedance of the nonlocal voltage signal (with lead resistance neglected). Eq. (2) implies a linear relation between R_0 and I/I_{NL}: $R_0 = R_{NL}(I/I_{NL}) - R_s$. Indeed, as we changed R_0 from 0 to 2 MΩ, R_0 v.s. I/I_{NL} fell on a straight line, whose slope and intercept yielded a measurement of R_{NL} and R_s, respectively (Fig. S2d). We noted that the R_{NL} obtained this way agreed with that from independent measurements described in Section I under the same condition. The R_s of 0.5 MΩ also agreed with the sample resistance between the nonlocal probes determined separately. The fact that R_{NL} and R_s were independent of excitation current (Fig. S2d) corroborate our finding that no sample heating occurred during the measurement.

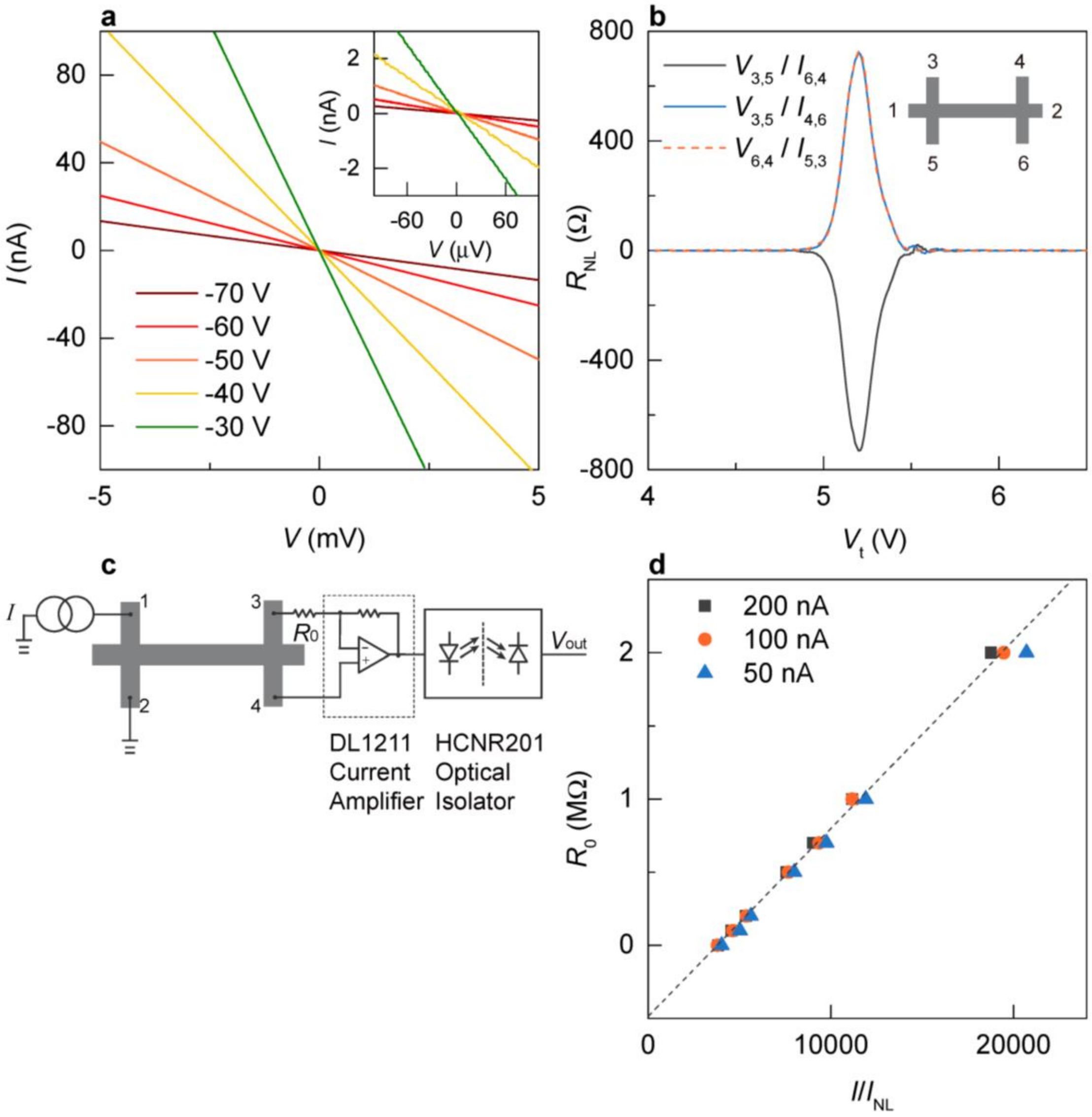

Supplementary Figure 2 | Nonlocal voltage signal characterization. **a**, Two-terminal I-V characteristics at CNP of a BG under varying gate-biases. Inset: zoomed in view of the I-V characteristics at low-biases. Linear I-V indicates ohmic contacts. Data were taken from the same sample and under the same condition as in Figure 2 in the main text. $T = 70$ K. **b**, Nonlocal signal measurement with reversed current (black and blue), and with voltage and current leads swapped (blue and orange). Measurement was performed at $T = 30$ K with V_b kept at -50 V. **c,** Nonlocal current measurement circuit with an external resistor R_0 added in series with the nonlocal voltage output. **d**, R_0 plotted as a function of I/I_{NL} for excitation current of 200 nA (black), 100 nA (orange) and 50 nA (blue). The broken line is a linear fit to the data.

III. Additional sets of nonlocal measurement

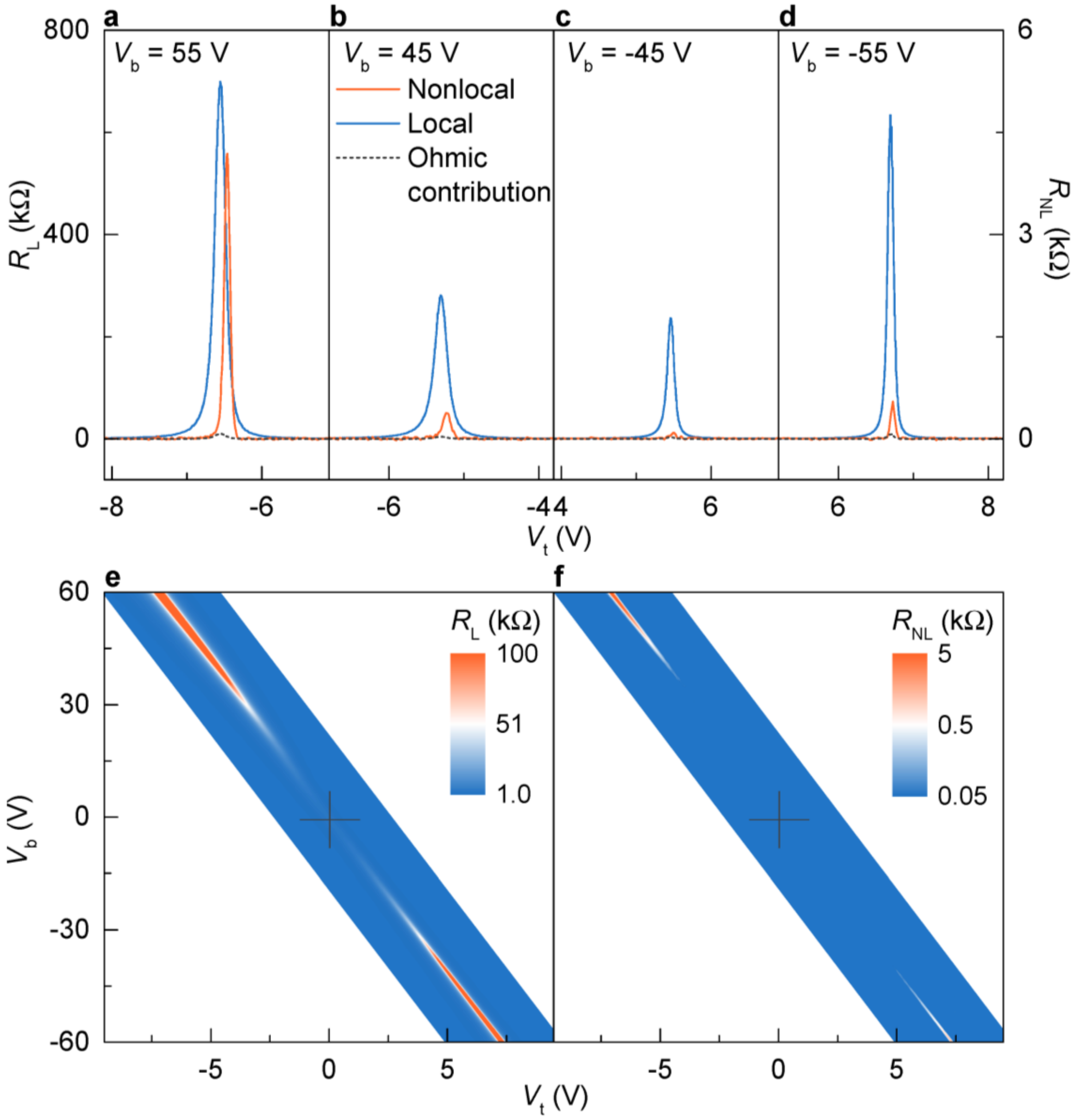

Supplementary Figure 3 | Local and nonlocal response of a biased BG different from the one shown in Fig. 2. a-d, Local and nonlocal resistance as a function of V_t with V_b fixed at different values. The length and width of the sample are 4 μm and 1.5 μm, respectively. Broken lines show expected ohmic nonlocal contribution, which is again much smaller than the observed R_{NL} (orange). We note that the peaks in R_{NL} are not aligned with peaks in R_L. Such misalignment was sample dependent, and we found it most likely due to inhomogeneity present in some of our BG samples (see section IV). **e** and **f**, local and nonlocal resistance measured as a function of both V_t and V_b. Data were taken on the same device measured in **a-d**. The crosses mark the point (V_{t0}, V_{b0}) $= (0.035\ \mathrm{V}, -0.7\ \mathrm{V})$, where no bandgap is opened in BG. All data were recorded at $T = 40$ K from the same sample shown in Fig. 3 a-c in the main text.

IV. Role of sample inhomogeneity

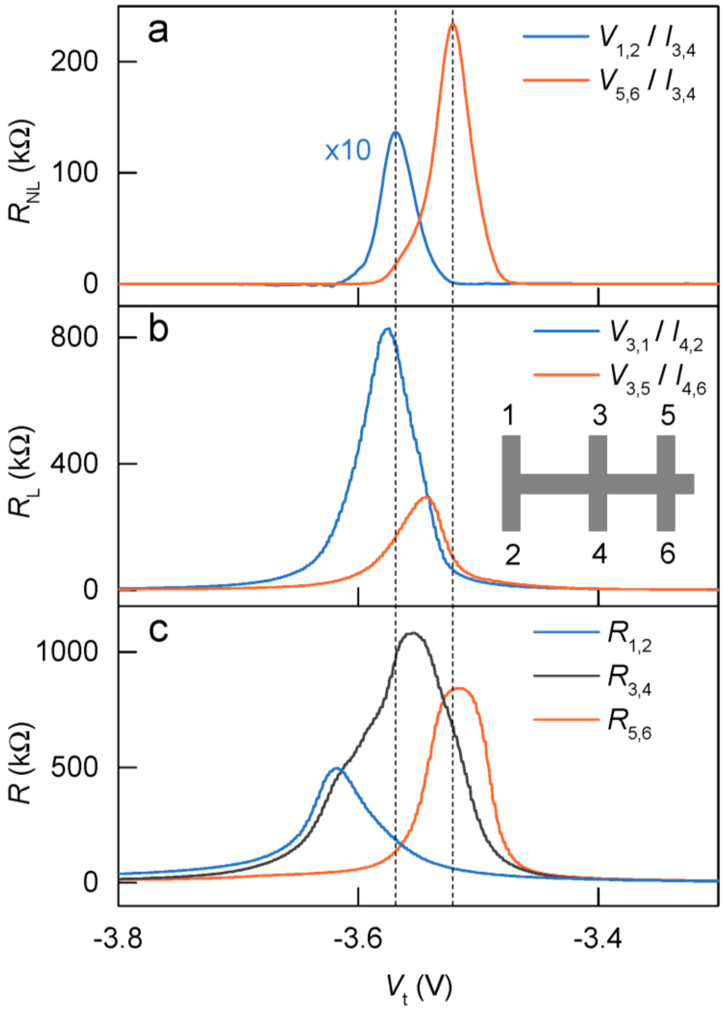

Supplementary Figure 4 | Sample inhomogeneity manifested as shift of resistance peaks at CNP. a and **b**, Nonlocal and local resistance, respectively, of the same sample measured in Fig. 3e. **c**, Two-terminal resistance R of the same sample as in **a** and **b**. A schematic of the device is shown in the inset of **b**. The broken lines mark the nonlocal peak positions. The different peak position in R_L and R obtained from different parts of the sample is a result of sample inhomogeneity[2]. The peaks in R_{NL} appear at positions close to peaks in R_L and R measured in similar part of the sample, pointing to sample inhomogeneity as the common origin of the peak position variations in R_{NL}, R_L and R.

V. Thermally activated and hoping transport in bilayer graphene

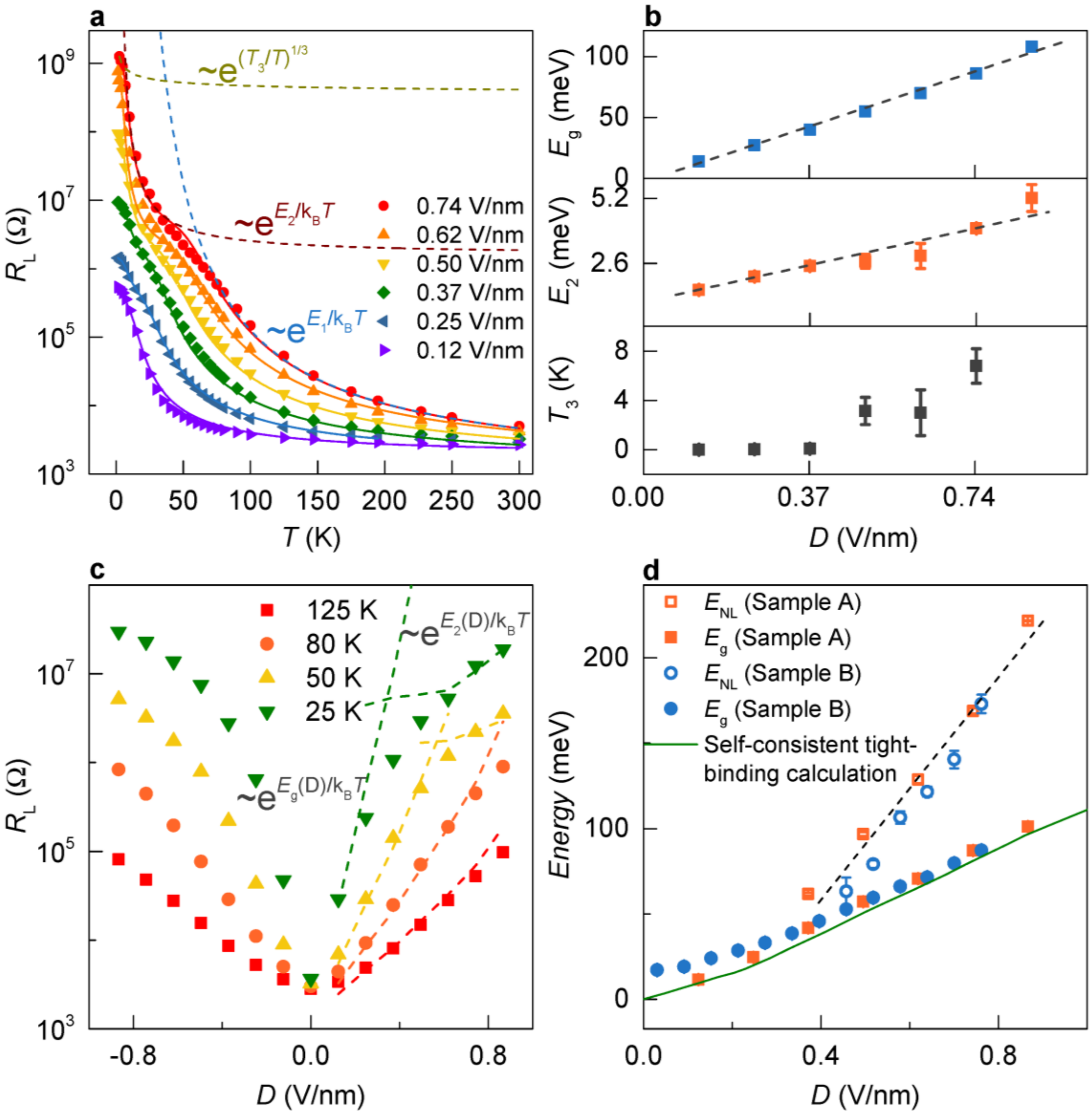

Supplementary Figure 5 | Temperature-dependent local and nonlocal transport in BLG. a, R_L as a function of temperature at varying electric displacement fields. The same set of data was shown in Fig. 3a in the main text. The behaviour of the observed R_L agreed well with that reported in ref 3–5, and all the data sets can be well fitted with the relation $R_L^{-1} = R_1^{-1}exp\left(-E_g/2k_BT\right) + R_2^{-1}exp\left(-E_2/k_BT\right) + R_3^{-1}\exp\left[-(T_3/T)^{1/3}\right]$, where the three terms correspond to contributions from thermal activation, nearest-neighbor hopping and variable-range hopping, respectively[4] (solid lines are the fitting results). We obtained energy scales E_g, E_2 and k_BT_3 from the fitting, and R_1, R_2 and R_3 are free parameters. E_g gives a measurement of BLG band gap; E_2 is the nearest-neighbor hopping energy; and T_3 is the onset temperature of variable-range hopping conduction. The broken lines represents individual contributions from thermal activation, nearest-neighbor hopping and variable-range hopping obtained from the fitting. **b**, E_g, E_2 and k_BT_3 as functions of D obtained from the fitting in **a**. Both E_g and E_2 increase linearly with D, and the broken lines are guide to the eye. Finite contribution from variable-range hopping appeared at $D \geq 0.5\ \mathrm{V/nm}$. These results are consistent with those reported in ref 3–5. **c**, Peak values of R_L at CNP measured as a function of D. At low temperatures (25 K and 50 K), the transport is dominated by thermal activation and nearest-neighbour hoping at low D and high D, respectively. Both thermal activation and nearest-neighbour hoping give exponential dependence of R_L on D, and the broken lines are plots of the two contributions with parameters obtained from fitting in **a**. At high temperatures ($\mathrm{T} \geq 80$ K), thermal activation alone dominated the transport at all D. **d**, E_g (solid symbols) and the exponent E_{NL} of nonlocal transport in the thermal activation regime (empty symbols) plotted as a function of D. Data were obtained by fitting of the slope at the linear part in the inset of Fig. 3a and 3b. The data were obtained from two samples: sample A is the same sample shown in Fig. 3a-c; sample B is the same sample shown in Fig. 2. The measured E_g agrees well with the BLG bandgap calculated with self-consistent tight-binding method (solid green line). The broken line is a linear fit to E_{NL}. E_{NL} is much larger than E_g, probably because the power law relation between R_{NL} and R_L: $R_{NL} \sim R_L^{\alpha}$. Indeed, the slope of E_{NL} is ~2.8 times larger than that of E_L, which is consistent with $\alpha = 2.77 \pm 0.02$ obtained from the scaling between R_{NL} and R_L (see main text).

VI. Sample dependence of the scaling between R_{NL} and R_L

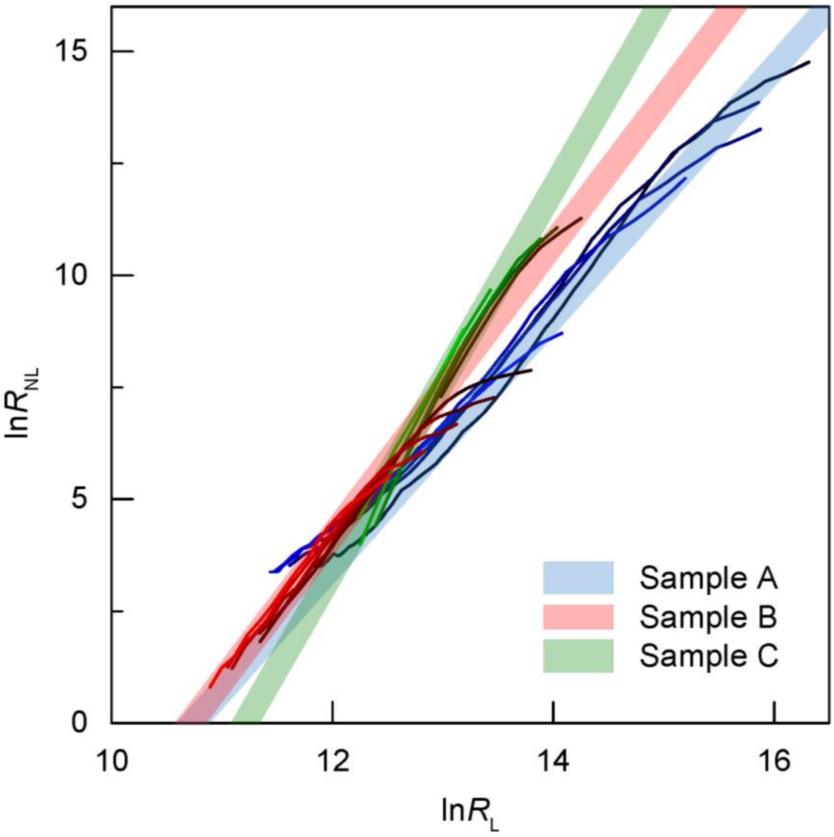

Supplementary Figure 6 | Sample-dependent scaling between R_{NL} and R_L. $\ln R_L$ plotted against $\ln R_{NL}$ at varying displacement field D. Date from three different samples are shown, with sample A the sample shown in Fig. 3c. The displacement fields are: $D = 0.37$ V/nm to 0.86 V/nm in 0.12 V/nm steps (red to black) for sample A; $D = 0.52$ V/nm to 0.76 V/nm in 0.061 V/nm steps (blue to black) for sample B; $D = 0.35$ V/nm to 0.83 V/nm in 0.12 V/nm steps (green to black) for sample C. The power law relation $R_{NL} \sim R_L^{\alpha}$ described all three data sets with the fitted value of α at 2.77, 3.26 and 4.27 in sample A, B and C, respectively. The curves all leveled off deep in the hopping regime, and those part of the curves was not included in the fitting.

VII. High-temperatures local and nonlocal transport in different samples

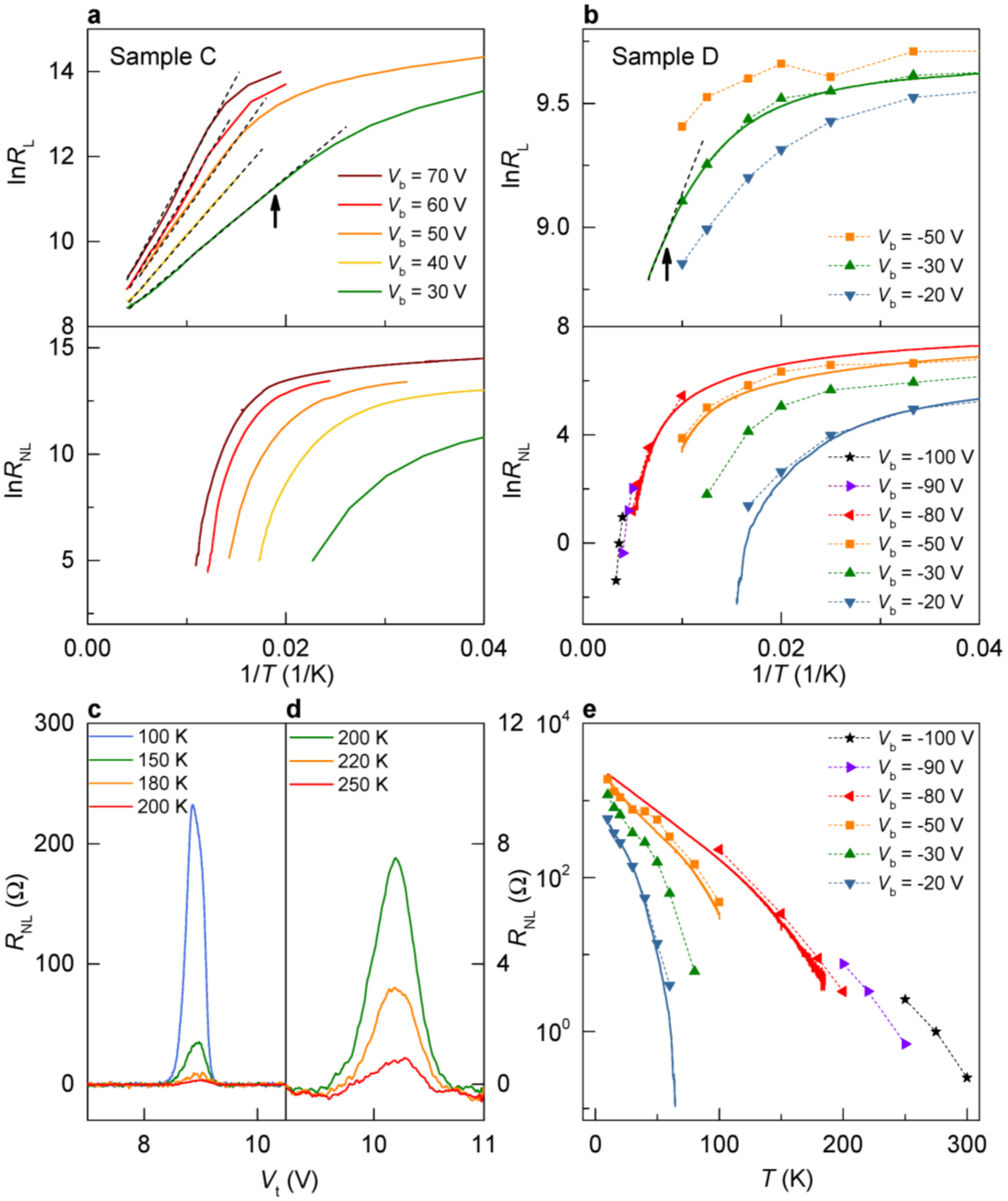

Supplementary Figure 7 | Thermally activated transport at high temperatures in different samples. a and **b**, Arrhenius plots of peak resistance of R_{NL} and R_L at CNP as functions $1/T$ for sample C and D (sample D is the same sample shown in Fig. 3d). The solid lines were obtained by sweeping temperature at CNP, and the scattered data points were obtained from gate sweeps at fixed temperatures. The black broken lines are linear fit in the thermal activation regime. The onset of the hopping regime (black arrows) is different in the two samples under comparable electric displacement fields. In both samples, R_{NL} decreased slowly with increasing temperature in the hopping regime, and dropped rapidly to 0 in the thermal activation regime. Such behaviour is consistent with the substantially different energy scale E_g and E_2 (Supplementary Section V). High temperature operation is therefore possible in samples with high onset temperature. **c**, High temperature R_{NL} measurement in sample C at $V_b = -80$ V. Finite R_{NL} persisted up to 200 K. **d**, High temperature R_{NL} measurement in sample C at $V_b = -90$ V. Finite R_{NL} was observed up to 250 K. **e**, Peak R_{NL} at CNP as a function of temperature obtained from sample D. Finite R_{NL} persisted up to 300K at $V_b = -100$ V.

VIII. Absence of nonlocal signal in monolayer graphene

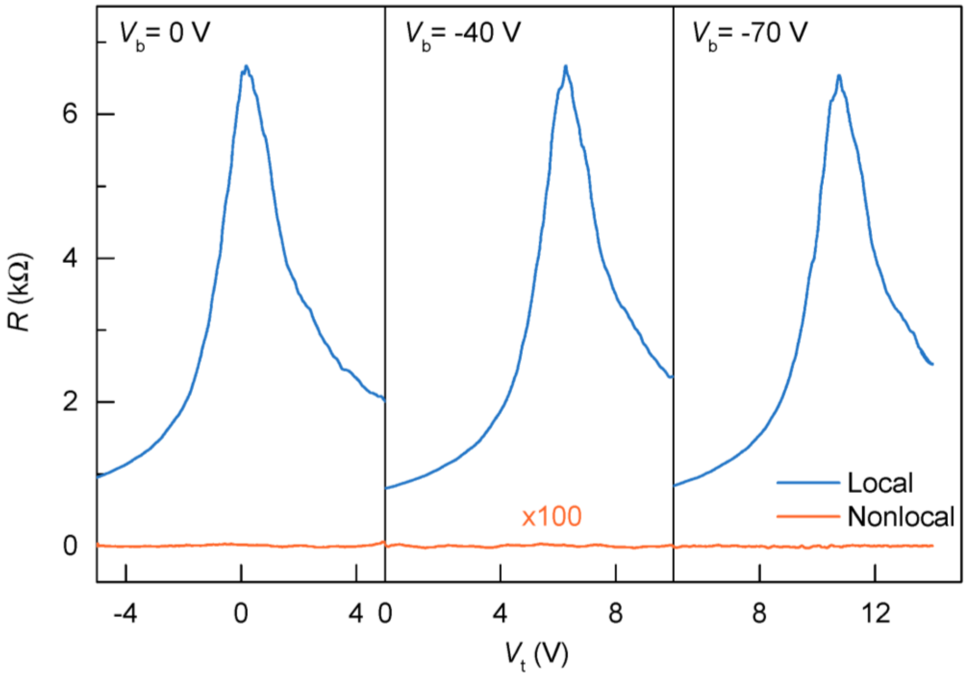

Supplementary Figure 8 | Local and Nonlocal measurement in monolayer graphene. Monolayer graphene FET with dual-gate structure was fabricated with the same procedure discussed in Methods. The length-to-width ratio is $\mathrm{L/w} = 5$, and the mobility is approximately $5000\ \mathrm{cm^2V^{-1}s^{-1}}$ at 10 K. The local and nonlocal resistance (blue and orange, respectively) were recorded at $V_b = 0$ V, -40 V and -70 V, covering the typical range of gate electric field that we used in BLG measurements. The peak value of local resistance did not change with gate, and we observed zero nonlocal response, to the best of our measurement resolution ($< 1\ \Omega$), for all the applied gate electric fields. The absence of nonlocal response in gate-biased monolayer graphene highlight the crucial role of gate-induced symmetry breaking in the nonlocal transport in BLG.

X. References

S1. Renard, J., Studer, M. & Folk, J. A. Origins of Nonlocality Near the Neutrality Point in Graphene. *Phys. Rev. Lett.* **112,** 116601 (2014).

S2. Blake, P. *et al.* Influence of metal contacts and charge inhomogeneity on transport properties of graphene near the neutrality point. *Solid State Commun.* **149,** 1068–1071 (2009).

S3. Zou, K. & Zhu, J. Transport in gapped bilayer graphene: The role of potential fluctuations. *Phys. Rev. B* **82,** 081407 (2010).

S4. Zhu, J. Transport in bilayer and trilayer graphene: band gap engineering and band structure tuning. in *http://meetings.aps.org/link/BAPS.2014.MAR.B30.1*

S5. Taychatanapat, T. & Jarillo-Herrero, P. Electronic Transport in Dual-Gated Bilayer Graphene at Large Displacement Fields. *Phys. Rev. Lett.* **105,** 166601 (2010).